In-situ formation of hydroxylated Ag active sites over Ag/MnO$_2$ modified by alkali metals for stable decomposition of ozone under humid conditions

Xiaotong Li [a,b], Jinzhu Ma [a,b,*], Guangzhi He [a,b], Zhisheng Wang [a,b], Hong He [a,b,*]

[a] *State Key Joint Laboratory of Environment Simulation and Pollution Control, Research Center for Eco-Environmental Sciences, Chinese Academy of Sciences, Beijing 100085, China*
[b] *University of Chinese Academy of Sciences, Beijing 100049, China*

ARTICLE INFO

ABSTRACT

Ag/MnO$_x$ catalysts have great prospects for practical application in ozone decomposition due to their excellent activity and water resistance; yet, improving the stability of Ag/MnO$_x$ catalysts for ozone decomposition remains challenging. Here, the addition of alkali metals significantly improved the stability of 2%Ag/MnO$_2$ catalyst for ozone decomposition under humid conditions. Alkali metals donate electrons to Ag nanoparticles through oxygen bridges, forcing Ag active sites to become hydroxylated by promoting the dissociation of H$_2$O molecules, and finally forming new stable hydroxylated Ag active sites (Ag-O(OH)$_x$-K). The O$_2^{2-}$ species on the new active sites of the 2%K-2%Ag/MnO$_2$ catalyst can easily desorb; therefore, the hydroxylated active sites can remain stable. These factors are key to the stable ozone decomposition activity of 2%K-2%Ag/MnO$_2$ catalyst in humid gas. This study represents a critical step towards the design and synthesis of high-stability catalysts for ozone decomposition.

1. Introduction

In recent years, continuously increasing ozone (O$_3$) levels originating from photochemical reactions between nitrogen oxides (NO$_x$) and volatile organic compounds (VOCs) have seriously endangered public health and the entire ecosystem in China [1,2]. It is very difficult to control O$_3$ pollution by controlling NO$_x$ and VOCs because of the nonlinear relationship between O$_3$ and the precursors [3,4]. Due to air exchange, the increase in O$_3$ concentration in the atmosphere will lead to an increase in indoor O$_3$ concentration [5]. Some emerging air purification equipments, such as disinfection equipment, negative-ion generators and electrostatic precipitators, are also important sources of indoor O$_3$ [6]. The cabins of aircraft flying at high altitudes also face O$_3$ pollution problems [7,8]. In addition, the tail gas from drinking water purification, disinfection and sterilization in the food industry and hospitals, removal of organic pollutants in wastewater, oxidation and absorption of industrial waste gas containing NO$_x$ and SO$_2$ and other processes contains a large amount of residual O$_3$, thus causing O$_3$ pollution [4,9,10]. The World Health Organization has set a guideline value of 100 ug/m^3 for the 8-hour average O$_3$ concentration and added a peak seasonal average O$_3$ concentration of 60 ug/m^3 in 2021 based on

the effects of long-term O$_3$ exposure on the total mortality rate and the mortality rate from respiratory diseases. Therefore, high-efficiency O$_3$ removal technology is urgently needed for air purification in the atmospheric environment and confined spaces and for the treatment of industrial tail gases.

Among the various O$_3$ removal methods, catalytic decomposition over manganese oxides, especially MnO$_2$, has attracted widespread attention due to its safety, high efficiency and low cost [4, 11–19]. The density of oxygen vacancies, as the main active sites of MnO$_2$ for ozone decomposition, is strongly related to the catalytic activity of MnO$_2$. Numerous methods have been implemented to increase the content of oxygen vacancies, such as doping with other metal elements [11,12,20, 21], regulating the content and type of ions in the tunnels of MnO$_2$ [22, 23], and vacuum deoxidation [14], which solved the problem of insufficient active sites and significantly enhanced the activity of MnO$_2$. However, water molecules will occupy part of the oxygen vacancies under a wet atmosphere, resulting in a serious decrease in activity [12]. Fabricating specific non-oxygen vacancy sites for H$_2$O adsorption [18], encapsulating MnO$_2$ within a hydrophobic layer [15,24], and creating water-resistant oxygen vacancies by chlorine introduction [25] have been applied to solve the problem of competitive adsorption of H$_2$O

molecules and O_3 molecules. Still, MnO_2 catalysts still face a serious challenge in that the accumulation of intermediate oxygen species on oxygen vacancies leads to a decrease in O_3 decomposition activity over time [12,26]. O_3 decomposition reaction is a typical redox reaction, and whether the intermediate oxygen species can easily desorb determines the stability of catalysts for O_3 decomposition. When the intermediate oxygen species desorb, the active site acts as an electron acceptor, and electrons are transferred from the intermediate oxygen species to the active site. Zhu et al. [15] regulated the electronic structure of oxygen vacancies to accelerate the desorption of intermediate oxygen species by encapsulating α-MnO_2 nanofiber within a graphene layer. Besides, whether O_3 molecules can be easily adsorbed/activated determines the activity of catalysts. When O_3 molecules are adsorbed, the active site acts as an electron donor, and electrons are transferred from the active site to the O_3 molecules [27,28]. Qu et al. [29] adjusted the electronic structure of Co species to promote the adsorption/activation of O_3 molecules by the electronic metal-support interaction of Co-C bonds in Co@NCNT. In summary, the activity and stability of catalysts for O_3 decomposition can be significantly improved by adjusting the electronic structure of the active site.

In our previous works, Ag as a high-efficiency active site for O_3 decomposition has been used to improve MnO_x, significantly enhancing the water resistance and activity of catalysts [30–32]. However, Ag/MnO_x catalysts still have the problem of slow deactivation caused by the non-desorption of intermediate oxygen species on metallic Ag nanoparticles (Ag_n^0), oxidizing and dispersing Ag_n^0 into small oxidized Ag clusters ($Ag_n^{\delta+}$) [31,32]. Therefore, accelerating the desorption of intermediate species that poison Ag active sites during O_3 decomposition and improving the stability of the physical and chemical states of high-efficiency Ag active sites in an O_3 atmosphere is key to improving the stability of Ag/MnO_x catalysts, which can be achieved by modulating the electronic structure of Ag active sites to accelerate electron transfer between intermediate oxygen species and active sites.

The addition of alkali metals can improve the activity and selectivity of Pt, Pd, Au and Ag-based catalysts in heterogeneous catalytic reactions, such as positive and reverse water gas shift conversion, CO oxidation, propylene oxidation and formaldehyde oxidation. The reasons why alkali metals improve the catalytic performance of Pt, Pd and Au-based catalysts are relatively clear, and can be mainly divided into the following categories: (1) Alkali metals interact with catalytically active sites as electron donors, which can weaken or enhance the bonding between the active metal and reactant molecules, thereby regulating the adsorption energy of reactants and intermediate species [33–35]. (2) Alkali metals interact with the metal atom of active sites via the surrounding oxygen atoms, stabilizing small metal nanoparticles or even atomically dispersing metal sites, finally opening up new reaction pathways [36–41]. Based on the above summary, alkali metals can donate electrons to Ag active sites and regulate the adsorption energy of the reactants and intermediate species on Ag species, which may solve the problem of non-desorption of intermediate species on the sites. Alkali metals may also interact with the metal atom of active sites via the surrounding oxygen atoms, stabilizing the valence state and size of Ag active sites or forming a new active site, solving the problem of the instability of Ag species during O_3 decomposition. Thus, the addition of alkali metals is expected to improve the stability of Ag/MnO_x catalysts for O_3 decomposition. Besides, the reason why alkali metals improve the O_3 decomposition performance of Ag/MnO_x catalysts remains to be determined.

In this study, the stability of 2%Ag/MnO_2 catalyst for O_3 decomposition was successfully improved by adding alkali metals (K, Rb and Cs). The interaction mechanism between alkali metals and Ag nanoparticles, the effect of alkali metals on the physicochemical state of Ag nanoparticles, and the essential reasons for the improvement of the stability of 2%Ag/MnO_2 catalyst were also proved, which provides guidance for the design and synthesis of high-stability catalysts for O_3 decomposition.

2. Experimental section

2.1. Preparation of catalysts

Preparation of MnO_2: 0.275 g of $MnSO_4 \cdot H_2O$ was added to 80 mL deionized water, then 1.5 g of $KMnO_4$ was added to the above solution, followed by stirring for about 1 h to make the solution homogeneous. Then, the mixed solution was moved to a 100 mL autoclave, sealed and kept at 240 °C for 24 h in an oven. Finally, the obtained black product was filtered, washed, dried overnight at 100 °C, and calcined at 500 °C for 2 h to obtain MnO_2.

Preparation of 2%Ag/MnO_2, 2%K (Rb or Cs)− 2%Ag/MnO_2, 2%Cs/ 2%Ag/MnO_2, and 2%Ag/2%Cs/MnO_2: the 2%Ag/MnO_2 catalyst was prepared by impregnating MnO_2 with $AgNO_3$ solution. 2%K (Rb or Cs)− 2%Ag/MnO_2 catalysts were prepared by impregnating MnO_2 with $AgNO_3$ solution and KNO_3 ($RbNO_3$ or $CsNO_3$) solution simultaneously. The 2%Cs/2%Ag/MnO_2 catalyst was prepared by impregnating MnO_2 with $AgNO_3$ solution and calcining, and then impregnating the product with $CsNO_3$ solution and calcining again. The 2%Ag/2%Cs/MnO_2 catalyst was prepared by impregnating MnO_2 with $CsNO_3$ solution and calcining, and then impregnating the product with $AgNO_3$ solution and calcining again. The detailed preparation steps of 2%Ag/MnO_2, 2%K (Rb or Cs)− 2%Ag/MnO_2, 2%Cs/2%Ag/MnO_2, and 2%Ag/2%Cs/MnO_2 catalysts are presented in Supplementary data.

2.2. Catalyst characterization

The crystal structure of catalysts was determined by X-ray powder diffraction (XRD, Bruker D8-Advance) using Cu Kα radiation (λ = 0.15406 nm) at 40 kV voltage and 40 mA current. The scanning range and step size were 10–90° and 0.02°, respectively. The N_2 adsorption and desorption curves of catalysts were measured by a Micromeritics 2460 surface area analyzer at 77 K. The morphology of catalysts was observed by field emission scanning electron microscopy (HITACHI, SU8020) and high-resolution transmission electron microscopy (JEOL, JEM-2100). The acceleration voltages used were 3 kV and 200 kV, respectively. The valence states and relative surface contents of Ag, Mn and O elements were determined by X-ray photoelectron spectroscopy (Axis Ultra, Kratos Analytical Ltd.). During the quasi-in-situ XPS test, 2% K-2%Ag/MnO_2 catalyst was treated in humid N_2 gas. The valence states and coordination of Ag elements on the catalysts were determined by XANES and EXAFS of the Ag K-edge at BL14W1 station of the Shanghai synchrotron radiation source. The in situ diffuse reflectance infrared Fourier transform spectroscopy (DRIFTS) of NH_3 adsorption was obtained on a Nexus 670 (Thermo Nicolet iS50) FTIR equipped with an MCT/A detector. A background spectrum was subtracted from each spectrum. In-situ Raman spectra were measured in a catalyst cell reactor system (CCR1000, Linkam Scientific Instruments) with a laser microconfocal Raman spectrometer (InVia Reflex, Renishaw). The gas flow rate was 50 mL/min, and the inlet O_3 concentration was about 5000 ppm. Spectra were acquired under oxygen flow and under an ozone/ oxygen mixture flow at the reaction temperature of 10 °C.

2.3. DFT calculations

In order to theoretically reveal the electron-donating effect of alkali metals on Ag/MnO_2 catalysts, the formation energy and electronic structure of catalysts were studied by density function theory (DFT). A slab model of Ag_2O with 24 Ag atoms and 12 O atoms was constructed through an optimized Ag_2O unit cell with lattice parameters of 4.79 Å, 4.79 Å and 4.79 Å. Then, the K atoms were anchored at different sites on the Ag_2O slab model. During the geometrical optimization, the bottom Ag_2O layer was kept frozen at its bulk positions, whereas all other atoms were fully relaxed. The crystal plane, supercell size and vacuum layer of the slab model were set to (100), 2 × 2 and 15 Å, respectively. All the DFT calculations were performed by the Vienna ab initio simulation

package (VASP) [42] with the projector augmented wave (PAW) method [43]. The Perdew-Burke-Ernzerhof (PBE) [44] generalized gradient approximation (GGA) was adopted to describe the exchange-correlation interaction. The van der Waals (vdW) interaction was described by the DFT-D3 method [45]. The kinetic energy cutoff was set to 500 eV, and the force and energy convergence criteria were set to 0.02 eV/Å and 10^{-6} eV, respectively.

2.4. Catalyst Activity

A continuous-flow fixed-bed quartz reaction tube (inner diameter: 4 mm) was filled with 40–60 mesh particle samples to test the O_3 decomposition activity of the corresponding catalysts. The catalyst dosage was 50 mg, the gas flow rate was 1400 mL/min, and the weight space velocity was 1680 $L \cdot g^{-1} \cdot h^{-1}$. The temperature for activity evaluation was controlled at 30 °C. The relative humidity (RH) of the total gas flow was kept at 65% by adjusting the proportion of dry and wet gas flow, and the humidity was measured in real time by a hygrometer probe (HMP110, Vaisala OYJ). The concentration of O_3 generated by a low-pressure UV lamp was kept at 40 ± 2 ppm. An O_3 detector (Model 202, 2B Technologies) was used to detect the inlet and outlet concentration of O_3, and the ozone concentrations at the inlet and outlet were defined as C_{in} and C_{out}, respectively. The O_3 conversion of catalysts was calculated by the following formula (Eq. (1)):

$$O_3 \text{ conversion} = \frac{C_{in} - C_{out}}{C_{in}} \times 100\% \qquad (1)$$

3. Results and discussion

3.1. Ozone decomposition performance

Under conditions of 30 °C, dry atmosphere, and weight space velocity of 1680 $L \cdot g^{-1} \cdot h^{-1}$, the MnO_2 catalyst showed 86% conversion of 40 ppm O_3 after 6 h, but the catalyst rapidly deactivated under a RH of 65% (Figure S1), indicating that the MnO_2 catalyst has poor water resistance. After Ag was loaded on the MnO_2 support, the O_3 conversion of 2%Ag/MnO_2 catalyst increased to 92% under a RH of 65% (Fig. 1a), showing that Ag can greatly enhance the activity of the catalyst under a humid atmosphere. Although the 2%Ag/MnO_2 catalyst had excellent activity during the first 6 h under a RH of 65%, its activity slowly declined during long-term testing, and finally decreased to 8% after 60 h (Fig. 1b), suggesting that it had poor stability for ozone decomposition under a humid atmosphere. Interestingly, when alkali metals were added, the O_3 decomposition activity of 2%K-2%Ag/MnO_2, 2%Rb-2%Ag/MnO_2 and 2%Cs-2%Ag/MnO_2 stabilized at 83%, 84% and 82% after 60 h (Fig. 1b), respectively, indicating that the addition of K, Rb or Cs

can significantly improve the stability of 2%Ag/MnO_2 catalyst for O_3 decomposition. Compared with the O_3 decomposition stability of Ag-based and Mn-based catalysts in recent years (Table S1), it is known that the O_3 decomposition stability of the 2%K-2%Ag/MnO_2 catalyst is advantageous under ultra-high space velocity. In addition, the TOFs were calculated at 30 °C under a RH of 65% and summarized in Table S2, and the results indicated that the TOF of 2%K (Rb or Cs)− 2%Ag/MnO_2 (0.0096, 0.0092, or 0.0093 s^{-1}) was more than 13 times higher than that of 2%Ag/MnO_2 (0.0007 s^{-1}). Moreover, the loading sequence of Ag and alkali metals did not affect the O_3 decomposition activity, as shown in Figure S2 for 2%Cs-2%Ag/MnO_2, 2%Cs/2%Ag/MnO_2 and 2%Ag/2%Cs/MnO_2 catalysts. Specific surface area is an important factor in determining the catalytic activity for O_3 decomposition. When Ag and alkali metals were loaded on the MnO_2 support, the specific surface areas of 2%Ag/MnO_2, 2%K-2%Ag/MnO_2, 2%Rb-2%Ag/MnO_2 and 2%Cs-2%Ag/MnO_2 catalysts decreased (Figure S3 and Table S3), but their O_3 decomposition activity increased, which indicates that the specific surface area is not the decisive factor for O_3 decomposition.

The enhancement of the stability of the 2%Ag/MnO_2 catalyst for O_3 decomposition by alkali metals may be due to the interaction between the alkali metals and MnO_2 or Ag nanoparticles. The 2%K (Rb or Cs)/MnO_2 catalysts were prepared and evaluated for O_3 decomposition. Compared with MnO_2, the O_3 conversion of 2%K (Rb or Cs)/MnO_2 catalysts did not change with time (Figure S4). As shown in Fig. 1b, both the 2%K/MnO_2 and 2%Ag/MnO_2 catalysts had poor activity and stability for O_3 decomposition, while the 2%K-2%Ag/MnO_2 catalyst showed excellent stability for O_3 decomposition. Therefore, it can be concluded that the enhanced stability for O_3 decomposition was caused by the interaction between the Ag nanoparticles and alkali metals. The detailed interaction mechanism will be discussed later.

In order to further determine the role of MnO_2 support, the catalysts that Ag was supported on the inert metal oxides (Al_2O_3) and other active metal oxides (Mn_2O_3) were compared. As shown in Figure S5, the addition of alkali metals inhibited the O_3 decomposition activity of 2%Ag/Al_2O_3 and 2%Ag/Mn_2O_3 catalysts, indicating that the contribution of MnO_2 support to the O_3 decomposition activity of 2%K-2%Ag/MnO_2 catalyst cannot be ignored. The influence of MnO_2 support on the O_3 decomposition activity of 2%K-2%Ag/MnO_2 catalyst may be the contribution of its own activity and the regulation of Ag active sites through the interaction between Ag and support. The poor activity of MnO_2 (Fig. 1a) under the current harsh test conditions indicated that it is mainly used as a support to regulate the coordination structure and electronic structure of Ag active sites.
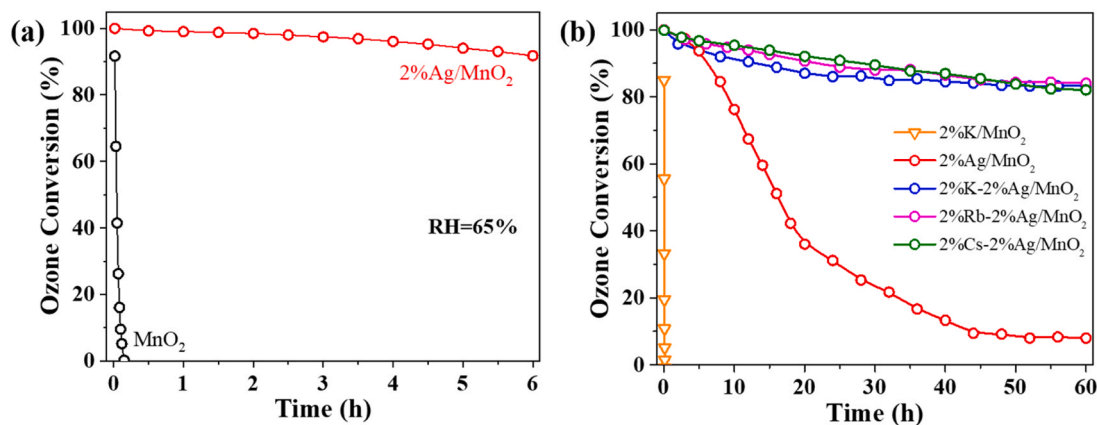
Fig. 1. O_3 conversion on (a) MnO_2 and 2%Ag/MnO_2 catalysts under a RH of 65%, (b) 2%K/MnO_2, 2%Ag/MnO_2, 2%K-2%Ag/MnO_2, 2%Rb-2%Ag/MnO_2, 2%Cs-2%Ag/MnO_2 catalysts under a RH of 65%. Conditions: O_3 inlet concentration 40 ppm, temperature 30 °C, weight space velocity 1680 $L \cdot g^{-1} \cdot h^{-1}$.

3.2. The states of Ag and the interaction between Ag nanoparticles and alkali metals

In order to determine the changes in the crystal structures of catalysts after the addition of Ag or alkali metal, XRD was used to characterize the catalysts. The XRD patterns of MnO_2 correspond to the standard PDF card of α-MnO_2 (44–0141) (Fig. 2a). Compared with the pure MnO_2 support, the diffraction peaks corresponding to MnO_2 on the 2%Ag/MnO_2 and 2%K (Rb or Cs)− 2%Ag/MnO_2 catalysts had no observable differences, and there were no diffraction peaks corresponding to Ag species or alkali metals on these catalysts, which may be because that the grain sizes of Ag species and alkali metals on these catalysts were small. When the K loading was increased to 8%, the diffraction peaks of metallic Ag were detected, corresponding to the increased size of Ag nanoparticles (Figure S9), indirectly proving the small grain size of Ag species on the 2%Ag/MnO_2 and 2%K (Rb or Cs)− 2%Ag/MnO_2 catalysts. EDS results demonstrated that the alkali metal was uniformly dispersed on these catalysts (Figure S10). Then, the Ag contents in 2% Ag/MnO_2, 2%K-2%Ag/MnO_2, 2%Rb-2%Ag/MnO_2 and 2%Cs-2%Ag/MnO_2 catalysts were determined to be 1.9, 1.8, 1.8 and 1.9 wt% (Table S4), respectively, which are basically consistent with the theoretical values. The content of K in MnO_2, 2%Ag/MnO_2, 2%Rb-2%Ag/MnO_2 and 2%Cs-2%Ag/MnO_2 catalysts is 6.5–6.8%, which is because $KMnO_4$ was used as the precursor during the preparation of MnO_2. K^+ is stable in the pore structure through coordinating with O atoms, which is a necessary condition for the formation of MnO_2 [46]. As shown by the activity data in Fig. 1b, it is clear that the K species in the pores cannot

improve the stability of Ag for O_3 decomposition. Compared with the 2% Ag/MnO_2 catalyst, the actual content of K in the 2%K-2%Ag/MnO_2 catalyst increased by 1.8 wt%, which was similar to the theoretical values. The actual contents of Rb and Cs in 2%Rb-2%Ag/MnO_2 and 2% Cs-2%Ag/MnO_2 catalysts are also consistent with their theoretical values.

In order to determine the size and morphology of Ag nanoparticles, the 2%Ag/MnO_2 and 2%K (Rb or Cs)− 2%Ag/MnO_2 catalysts were characterized by HRTEM. As shown in Fig. 2b-c and Figure S11, the average size of Ag nanoparticles on the 2%Ag/MnO_2 catalyst is 2.5 $\pm$ 1.1 nm. The average size of Ag nanoparticles on the 2%K-2%Ag/ MnO_2, 2%Rb-2%Ag/MnO_2 and 2%Cs-2%Ag/MnO_2 catalysts increased to 4.7 $\pm$ 1.5 nm (Fig. 2b, e and Figure S11), 4.1 $\pm$ 1.3 nm (Fig. 2b, g, and Figure S11) and 5.6 $\pm$ 1.6 nm (Fig. 2b, i, and Figure S11), respectively, which indicated that Ag nanoparticles agglomerate after the addition of alkali metals (Fig. 2b) [35]. Besides, the size of Ag nanoparticles gradually increased with the increase in the alkali metal loading (Figure S9). In previous studies [35,47], the alkali metals were found to promote the agglomeration of Ag particles and increased the content of metallic Ag species on Ag/Al_2O_3 catalysts, and it was speculated that the interaction between the alkali metals and Ag weakened the interaction between Ag and the Al_2O_3 support, thus causing the Ag precursors to decompose into the metallic state and agglomerate into large particles. As shown in Fig. 2d, the lattice fringes of Ag nanoparticles on 2%Ag/MnO_2 catalysts are regular and neat, while the lattice fringes of Ag nanoparticles on 2% K (Rb or Cs)− 2%Ag/MnO_2 catalysts are fuzzy and have various orientations (Fig. 2f, h and j), indicating there are more grain boundaries and
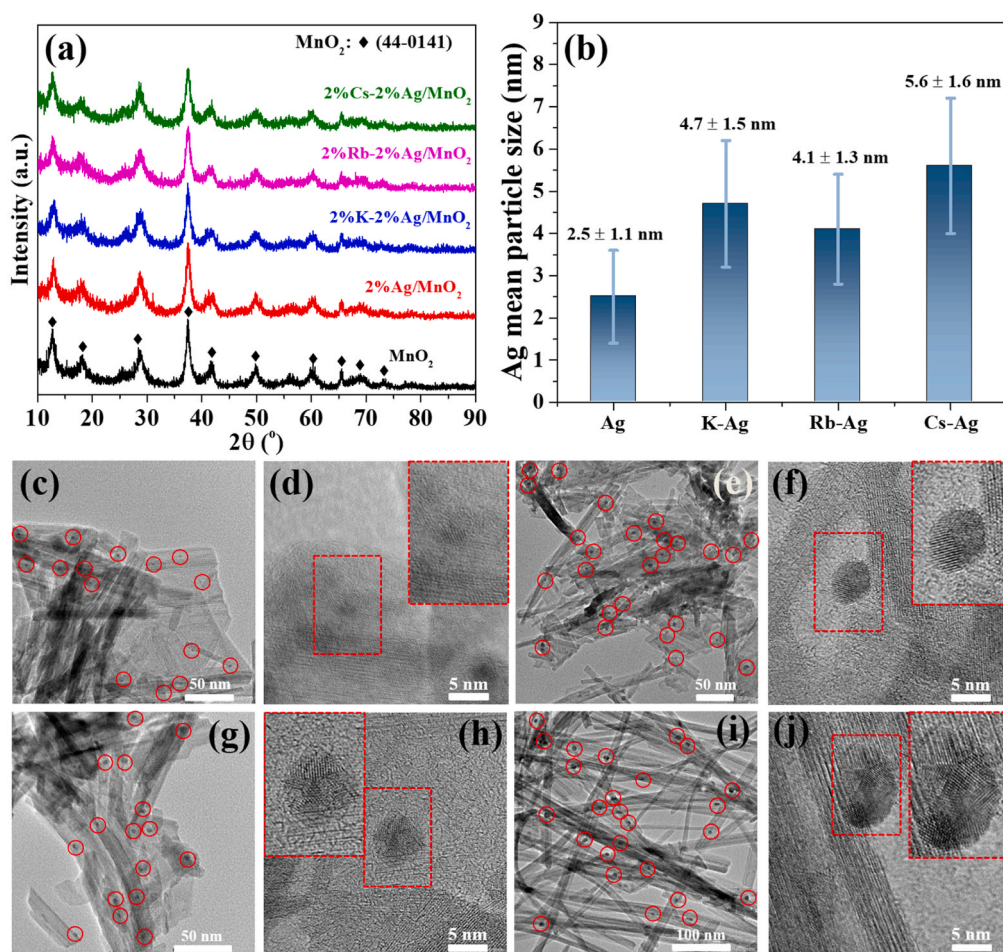
Fig. 2. (a) XRD patterns of MnO_2, 2%Ag/MnO_2, 2%K (Rb or Cs)− 2%Ag/MnO_2 catalysts; (b) The average size of Ag nanoparticles of 2%Ag/MnO_2 and 2%K (Rb or Cs)− 2%Ag/MnO_2 catalysts; HRTEM images of (c-d) 2%Ag/MnO_2, (e-f) 2%K-2%Ag/MnO_2, (g-h) 2%Rb-2%Ag/MnO_2, (i-j) 2%Cs-2%Ag/MnO_2.

amorphous regions on them [35,47]. Li et al. [48] found that the stacking faults in silver nanoparticles can cause a low coordination number and high tensile strain, thus improving the adsorption energy and transforming the non-active silver into a highly active catalyst. Therefore, more grain boundaries and amorphous regions on Ag nanoparticles should be beneficial to the improvement of O_3 decomposition activity of catalyst.

The valence states of Ag were determined by XPS spectroscopy. The Ag $3d_{5/2}$ binding energy of Ag^0 and Ag^+ are 368.50 and 367.50 eV, respectively [32,49]. For the 2%Ag/MnO$_2$ catalyst, the binding energy of Ag $3d_{5/2}$ is 367.56 eV (Fig. 3a), which is the same as that of Ag^+ (367.50 eV), indicating that the Ag nanoparticles on the catalyst are in the oxidized state. Ag$_2$O nanoparticles were later used to as a reference for Ag species on the 2%Ag/MnO$_2$ catalyst. For the 2%K-2%Ag/MnO$_2$, 2%Rb-2%Ag/MnO$_2$ and 2%Cs-2%Ag/MnO$_2$ catalysts, the binding energy of Ag $3d_{5/2}$ shifted to 368.00 eV, indicating that the Ag nanoparticles gain more electrons, which may be because the alkali metals (K, Rb or Cs) donate electrons to the Ag nanoparticles. Besides, the binding energy of Ag $3d_{5/2}$ gradually shifted in the direction of higher energy with an increase in the loading of alkali metal (Figure S9). The higher binding energy of Ag $3d_{5/2}$ suggests that Ag nanoparticles are closer to the metallic state, corresponding to the XRD results, in which the diffraction peaks of Ag^0 were detected for the 8%K-2%Ag/MnO$_2$ catalyst, and HRTEM results showing a gradually increasing particle size. As shown in Figure S12, with the increase in alkali metal loading, the size of Ag nanoparticles gradually increased, Ag nanoparticles were also closer to the metallic state, and the TOF of the x%K-2%Ag/MnO$_2$ catalysts gradually increased. The O_3 decomposition reaction occurs on the surface of Ag nanoparticles. The addition of alkali metal increased the particle size of the Ag nanoparticles, leading to a decrease in the number of exposed Ag active sites, which is not favorable to the O_3 decomposition reaction. However, the addition of alkali metal significantly enhanced the O_3 decomposition activity of the 2%Ag/MnO$_2$ catalyst, which is because the O_3 decomposition capacity of individual Ag active sites is enhanced due to the modulation of the electronic structure of the sites by alkali metals. Therefore, it can be concluded that the electronic structure of Ag active sites is the key to the improvement of the stability for O_3 decomposition.

In order to further reveal the electronic structure of Ag nanoparticles on catalysts, the Ag K-edge XAFS data of 2%Ag/MnO$_2$ and 2%K (Rb or Cs)− 2%Ag/MnO$_2$ catalysts were analyzed. As shown in Fig. 3b, compared to the 2%Ag/MnO$_2$ catalyst, the Ag K-edge energy and edge step of the 2%K (Rb or Cs)− 2%Ag/MnO$_2$ catalysts moved toward those of Ag foil. The above results further demonstrated that the alkali metals (K, Rb or Cs) regulate the electronic structure of Ag nanoparticles by donating electrons to Ag, which is consistent with the XPS results. In

conclusion, the change in the electronic structure of Ag active sites plays a key role in improving the stability of O_3 decomposition. However, the details of how the electronic structure of Ag active sites affects the stability of O_3 decomposition remain unclear. Therefore, further characterization was conducted to clarify the mechanism.

Many researchers have demonstrated that alkali metals can interact with noble metals (Pt and Au) via oxygen bridges to form Pt/Au-O(OH)-Na/K structures, thus stabilizing the active metal atoms [36,39]. Therefore, it is speculated that the alkali metals (K, Rb or Cs) also interact with Ag atoms through oxygen bridges on 2%K (Rb or Cs)− 2% Ag/MnO$_2$ catalysts, forming a similar Ag-O-K (Rb or Cs) structure.

The interaction between Ag atoms and alkali metals was analyzed by DFT calculations, with K as the representative alkali metal. K atoms are anchored to the S1 and S2 sites of Ag$_2$O, respectively (Figure S15). The simulated structures of Ag$_2$O and Ag$_2$O-K nanoclusters are presented in Figure S16 (top view) and Figure S17 (side view). The formation energies of Ag$_2$O-K-1 and Ag$_2$O-K-2 are − 3.33 eV and − 3.63 eV, respectively. The formation energy of Ag$_2$O-K-2 is lower, indicating that it is a more stable structure. The charges of several representative atoms (Figure S18) for Ag$_2$O and Ag$_2$O-K-2 are presented in the form of Bader charges (Table S5). The Bader charge is correlated with the valence of the individual ions, but is lower than the true valence because of the partial covalent interaction of the M-O bond [50]. As shown in Table S5, the Bader charges of Ag3, Ag6, Ag21 and Ag24 atoms bonding to the K atom via an oxygen bridge in the Ag$_2$O-K-2 structure are + 0.531, + 0.537, + 0.534 and + 0.534, which are lower than those of Ag atoms in the Ag$_2$O structure (+0.539, +0.540, +0.540 and +0.540), demonstrating the partial electron transfer from K to Ag atoms through adjacent oxygen atoms. The Ag3-O2, Ag24-O2, Ag6-O11 and Ag21-O11 bond lengths (2.02 Å) in the Ag$_2$O-K-2 structure are significantly longer than those in the Ag$_2$O structure (1.98 Å), corresponding to the lower valence state of Ag in the Ag$_2$O-K-2 structure. Therefore, the alkali metals transfer electrons to Ag nanoparticles through the oxygen bridges of the Ag-O-K (Rb or Cs) structures because of the electron donor effect of alkali metals.
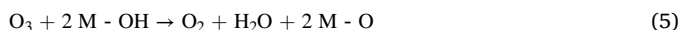
3.3. The essential reason for the improved stability of 2%Ag/MnO$_2$ for O$_3$ decomposition on the addition of alkali metals

Oyama et al. [26] have proposed the following O_3 decomposition mechanism of manganese oxide catalysts associated with peroxide species (Eqs. (2)–(4)):

$$O_3 + * \rightarrow O* + O_2 \tag{2}$$

$$O_3 + O* \rightarrow O_2* + O_2 \tag{3}$$
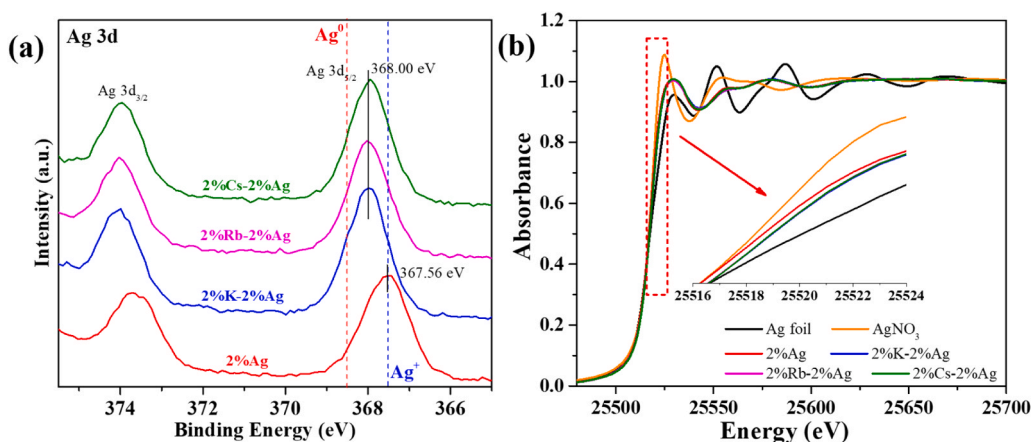
Fig. 3. (a) Ag 3d XPS spectra of 2%Ag/MnO$_2$, 2%K (Rb or Cs)− 2%Ag/MnO$_2$ catalysts; (b) Ag K-edge XANES spectra for Ag foil, AgNO$_3$, 2%Ag/MnO$_2$, 2%K (Rb or Cs)− 2%Ag/MnO$_2$ catalysts.

$$O_2^* \rightarrow O_2 + * \quad \text{(rate-limiting step)} \tag{4}$$

According to publications on the O_3 decomposition mechanism of Ag catalysts, compared with Co, Ni, Fe, and Mn oxides, the accumulated intermediate oxygen species on Ag catalysts during O_3 decomposition are different, because of the higher reactivity of accumulated oxygen species toward CO during O_3 decomposition [51]. Besides, in previous study, an O_3 decomposition process of metallic Ag involving atomic oxygen species, peroxide species, Ag_2O and AgO was speculated, but intermediate oxygen species have been not observed by reliable experimental methods [32, 52–54]. The above reaction mechanism on MnO_x and Ag catalysts determines that the accumulation of intermediate oxygen species on the catalyst surface will lead to the deactivation of catalysts. According to our previous research [55], the NiFe-LDH catalyst solves the deactivation problem of common O_3 decomposition catalysts by changing the active site and reaction mechanism. The hydroxyl groups on the NiFe-LDH catalyst are involved in the O_3 decomposition reaction (Eqs. (5)–(6)):

$$O_3 + 2 \text{ M - OH} \rightarrow O_2 + H_2O + 2 \text{ M - O} \tag{5}$$

$$2 H_2O + 4 \text{ M - O} \rightarrow O_2^* + 4 \text{ M - OH} \quad \text{(rate-limiting step)} \tag{6}$$

In this study, the slow deactivation of the 2%Ag/MnO_2 catalyst was solved by adding alkali metal, and the catalysts with added alkali metals had excellent stability for O_3 decomposition. The above results have demonstrated that the alkali metals regulate the electronic structure of Ag nanoparticles by donating electrons to Ag; however, whether the addition of alkali metals changes the active site or the reaction mechanism remains to be determined.

Interestingly, the O_3 decomposition activity of the 2%K-2%Ag/MnO_2 catalyst under RH of 30% and 65% is superior to that under dry gas (Fig. 4a), indicating that H_2O molecules can enhance the O_3 decomposition activity of this catalyst. Thus, H_2O molecules play an important role in the enhancement of the activity of the 2%K-2%Ag/MnO_2 catalyst in humid gas. As shown in Fig. 4b, when the 2%K-2%Ag/MnO_2 catalyst is exposed to water vapor, many hydroxyl groups are formed on the catalyst [56]. In situ DRIFTS results of NH_3 adsorption further proved

that surface hydroxyl groups were formed on 2%K-2%Ag/MnO_2 catalyst under humid gas (Figure S20) [57]. Combining these data with the DFT calculation results, H_2O molecules easily decomposed to *OH and *H on each type of adsorption site of Ag_2O-K (Figure S21 and Fig. 4c-e), where H atoms are adsorbed on the O sites and OH are adsorbed on the Ag sites, finally forming a layer of *OH on the surface. The calculation results well explain the formation of hydroxyl groups in humid gas. However, H_2O molecules are simply adsorbed on each type of adsorption site of Ag_2O and do not decompose (Figure S22). The above results indicate that Ag nanoparticles regulated by alkali metals promote the dissociation of H_2O molecules, which is related to the change in the electronic structure of Ag nanoparticles after alkali metal addition. Compared to Ag_2O, the distance between the Ag atom in Ag_2O-K and the O atom in the H_2O molecule shortens from 2.66 Å to 2.02 Å, and the distance between the O atom in Ag_2O-K and the H atom in the H_2O molecule shortens from 1.76 Å to 0.98 Å, indicating that the interaction of the O atom in Ag_2O-K and the H atom in the H_2O molecule is significantly enhanced, thus causing the breakage of the O-H bond in the H_2O molecule, promoting the dissociative adsorption of H_2O molecules. The enhanced interaction of the O atom in Ag_2O-K and the H atom in the H_2O molecule is mainly due to the more negative valence of O atom in Ag_2O-K resulting from the electron transfer of alkali metals (Table S5). The promotion effect of alkali metals on water dissociation has been also investigated on Cu/TiO_2, and it was concluded that K atoms favor the thermochemistry for water dissociation on Cu and Cu/TiO_2, with the cleavage of an O-H bond occurring at room temperature [58]. Therefore, the O_3 decomposition reaction under humid gas conditions occurs on the surface of hydroxylated Ag_2O-K, where we defined the hydroxylated Ag_2O-K model as Ag-O(OH)$_x$-K (Figure S23). Ag-O(OH)$_x$-K, as the new active site, can more reasonably represent the 2%K-2%Ag/MnO_2 catalyst in humid gas. However, once the introduction of H_2O is stopped, the O_3 decomposition activity of the 2%K-2%Ag/MnO_2 catalyst will decrease (Figure S24). Then, when the gas path is switched to 65% RH, the O_3 removal efficiency can be recovered quickly. The above results indicate that surface hydroxyl groups can be in-situ formed rapidly under humid gas but cannot exist stably under dry gas.
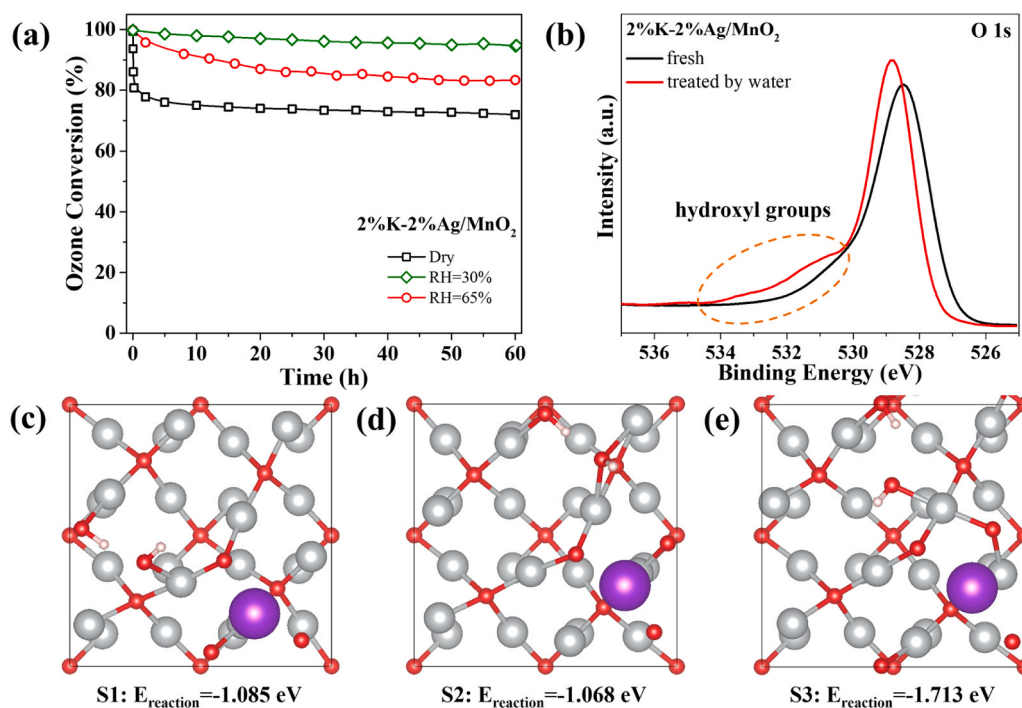

Fig. 4. (a) O_3 conversion on 2%K-2%Ag/MnO_2 catalyst under dry atmosphere and RH of 30% and 65%. Conditions: O_3 inlet concentration 40 ppm, temperature 30 °C, weight space velocity 1680 L·g^{-1}·h^{-1}. (b) The quasi-in-situ O 1s XPS spectra of 2%K-2%Ag/MnO_2 catalysts, which were not pre-treated or treated under humid gas; (c-e) DFT calculated results of reaction energy of H_2O decomposition on Ag_2O-K (Ag_2O-K represents 2%K-2%Ag/MnO_2).

The adsorbed intermediates on the 2%K-2%Ag/MnO$_2$ catalyst under dry gas and RH 65% during O$_3$ decomposition were studied by in-situ Raman spectroscopy. For the 2%K-2%Ag/MnO$_2$ catalyst, once O$_3$ is introduced under either dry gas or RH 65%, a new Raman peak representing O$_2^{2-}$ species will appear at 835 cm^{-1} (Fig. 5a and b). Moreover, the Raman signal of O$_2^{2-}$ was weaker under RH 65% than that under dry gas, indicating that O$_2^{2-}$ species on 2%K-2%Ag/MnO$_2$ desorb more easily under humid gas, which should be related to the formation of hydroxylated active sites. Ag$_2$O-K (Figure S18) and Ag-O(OH)$_x$-K (Figure S23) represent the active sites of the 2%K-2%Ag/MnO$_2$ catalyst under dry and humid gas, respectively. As shown in Fig. 5c and Figure S25, the desorption energy for O$_2^{2-}$ species on Ag-O(OH)$_x$-K (0.22 eV) is much lower than that on Ag$_2$O-K (0.70 eV), indicating that the desorption of O$_2^{2-}$ species on Ag-O(OH)$_x$-K is more likely to occur, corresponding to the weaker Raman signal of O$_2^{2-}$ on 2%K-2%Ag/MnO$_2$ under humid gas, so the 2%K-2%Ag/MnO$_2$ catalyst has better activity under humid gas. The hydroxyl groups on the NiFe-LDH catalysts are involved in the reaction as active sites, and the reaction mechanism of the catalysts is changed. However, the O$_3$ molecules still follow the decomposition path involving peroxide species on the in-situ-formed hydroxylated active sites on the 2%K-2%Ag/MnO$_2$ catalyst, but the peroxide species are more easily desorbed at the hydroxylated active sites, thus accelerating the O$_3$ decomposition process. In addition, the adsorption energy of O$_3$ on the active sites also reflects the O$_3$ decomposition activity of catalysts [27–29]. The adsorption of O$_3$ on Ag-O(OH)$_x$-K (−0.97 eV) is stronger than that on Ag$_2$O-K (−0.54 eV), so O$_3$ decomposition reaction is easier to occur on Ag-O(OH)$_x$-K, which is also a key factor that the 2%K-2%Ag/MnO$_2$ catalyst has higher O$_3$ decomposition activity under humid gas.

To further determine the reason for the difference in the stability of 2%Ag/MnO$_2$ and 2%K-2%Ag/MnO$_2$ catalysts for O$_3$ decomposition at RH of 65%, the adsorbed intermediates on the two catalysts were studied by in-situ Raman spectroscopy. The Raman signal of O$_2^{2-}$ was stronger on 2%Ag/MnO$_2$ than on 2%K-2%Ag/MnO$_2$ (Fig. 5d), indicating that O$_2^{2-}$ species on 2%Ag/MnO$_2$ are more difficult to desorb. The calculation results show that the structure of Ag$_2$O is unstable during the reaction process and cannot restore to the initial state after undergoing the O$_3$ decomposition reaction (Fig. 6a), corresponding to the agglomerated Ag nanoparticles with blurred lattice stripes observed on the used 2%Ag/MnO$_2$ catalyst (Fig. 7a, b, c and Figure S26). Liu et al. [59] also found that highly dispersed Ag nanoclusters spontaneously aggregated in humid O$_2$ atmosphere. Then, the changed Ag$_2$O species after undergoing the O$_3$ decomposition reaction is defined as (Ag$_2$O)', and the reaction energy of every step of O$_3$ decomposition on it was determined. Compared with Ag$_2$O and Ag-O(OH)$_x$-K, the desorption energy of O$_2^{2-}$ species on (Ag$_2$O)' increased to 0.36 eV (Fig. 6b), so the desorption of O$_2^{2-}$ species on it become more difficult, corresponding to the stronger Raman signal of O$_2^{2-}$ on 2%Ag/MnO$_2$, thus causing the worse O$_3$ decomposition activity of the 2%Ag/MnO$_2$ catalyst (Fig. 1b). The structure of Ag-O(OH)$_x$-K is stable and has no detectable change after the O$_3$ decomposition reaction (Figure S25), corresponding to the HRTEM results showing that the size and lattice fringes of Ag nanoparticles on 2%K-2%Ag/MnO$_2$ remain stable after reaction (Fig. 7a, d, e and Figure S26). The Ag and K contents on catalysts after long-term reaction were determined by ICP. After reacting for 60 h, the content of Ag on 2% Ag/MnO$_2$ catalyst is 1.8%, and the contents of Ag and K on 2%K-2% Ag/MnO$_2$ catalyst are 1.8% and 8.5%. Compared with the fresh catalyst, the contents of Ag and K on 2%Ag/MnO$_2$ and 2%K-2%Ag/MnO$_2$ catalysts have not changed, indicating that Ag and K elements will not be lost in the long-term reaction process. The change in the valence state of Ag
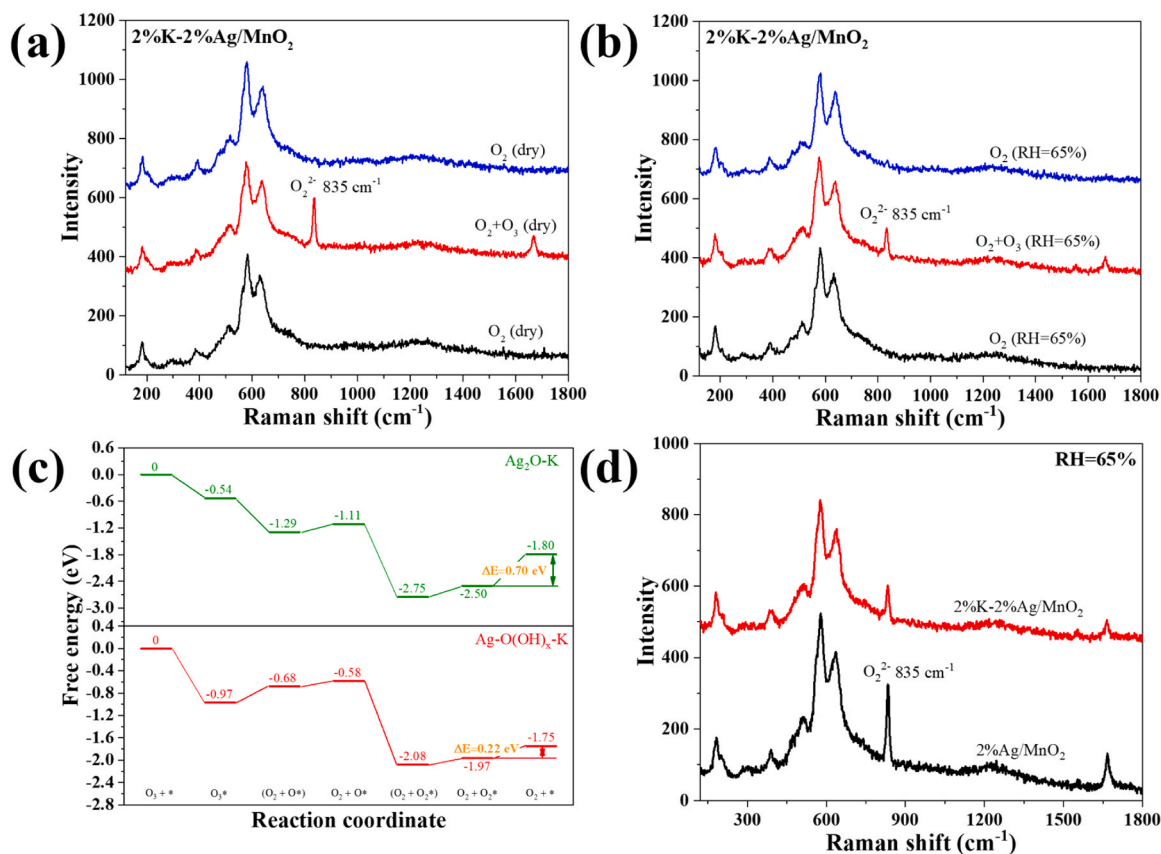
Fig. 5. In-situ Raman spectra of 2%K-2%Ag/MnO$_2$ catalyst under (a) dry gas and (b) RH= 65%; (c) Free energy diagram of Ag$_2$O-K and Ag-O(OH)$_x$-K towards O$_3$ decomposition reaction (Ag$_2$O-K and Ag-O(OH)$_x$-K represent the active sites of 2%K-2%Ag/MnO$_2$ under dry gas and humid gas, respectively); (d) In-situ Raman spectra of 2%Ag/MnO$_2$ and 2%K-2%Ag/MnO$_2$.
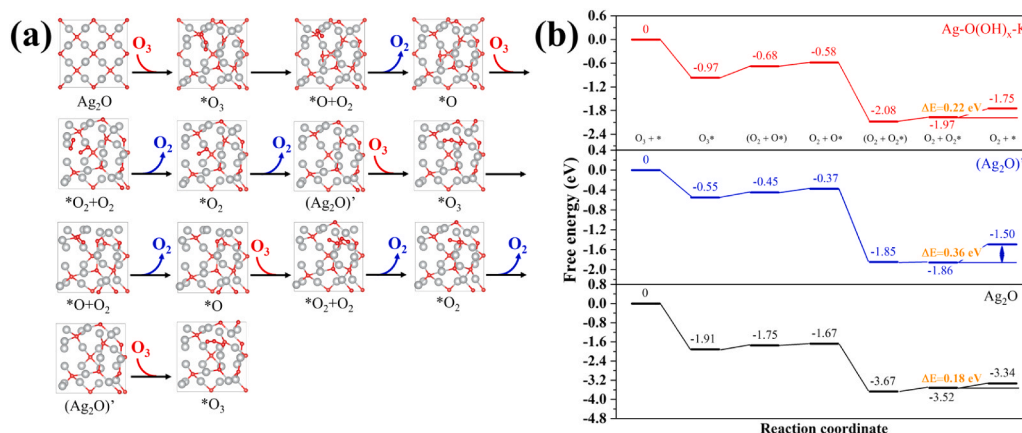
Fig. 6. (a) Proposed reaction scheme, with the intermediates having the optimized geometry of Ag_2O for the O_3 decomposition reaction (Ag_2O represents 2%Ag/MnO_2, $(Ag_2O)'$ represents the used Ag_2O under O_3 atmosphere); (b) Free energy diagram of Ag_2O, $(Ag_2O)'$ and Ag-O(OH)$_x$-K during the O_3 decomposition reaction.
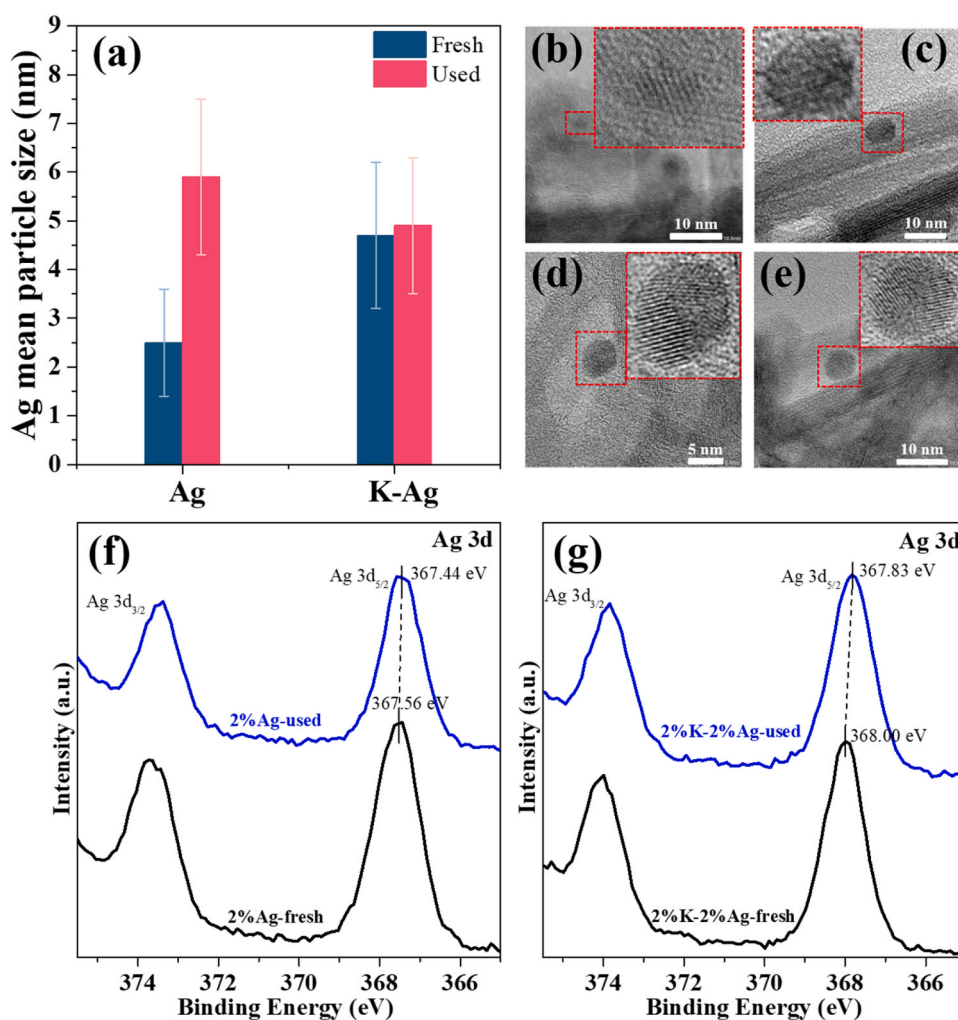
Fig. 7. (a) The average size of Ag nanoparticles on fresh and used 2%Ag/MnO_2 and 2%K-2%Ag/MnO_2 catalysts; HRTEM images of (b) fresh and (c) used 2%Ag/MnO_2 catalyst; (d) fresh and (e) used 2%K-2%Ag/MnO_2 catalyst; Ag 3d XPS spectra of fresh and used (f) 2%Ag/MnO_2 and (g) 2%K-2%Ag/MnO_2 catalysts.

nanoparticles after reaction was also determined by XPS. As shown in Fig. 7f and g, the binding energy of Ag $3d_{5/2}$ on 2%Ag/MnO_2 and 2% K-2%Ag/MnO_2 catalysts shows almost no change after reacting for 60 h, indicating that the valence state of Ag nanoparticles is relatively stable. Besides, compared with Ag_2O (−1.91 eV), the adsorption of O_3 on $(Ag_2O)'$ (−0.55 eV) is significantly weaker, which also explains the

unstable O_3 decomposition activity of 2%Ag/MnO_2 catalyst. The adsorption of O_3 on Ag-O(OH)$_x$-K (−0.97 eV) is also stronger than that on $(Ag_2O)'$ (−0.55 eV), so the O_3 decomposition activity of 2%K-2% Ag/MnO_2 catalyst is better than that of 2%Ag/MnO_2 catalyst after long-term reaction [27–29].

For the 2%Ag/MnO_2 catalyst, the physical and chemical states (size,

crystallinity, and valence state) of Ag nanoparticles are unstable during O_3 decomposition, and the O_2^{2-} species on the catalyst are more difficult to desorb than those on the 2%K-2%Ag/MnO_2 catalyst under humid gas, so its activity gradually declines during 60 h of activity testing. However, K donates electrons to Ag atoms through oxygen bridges, forcing Ag active sites to become hydroxylated by promoting the dissociation of H_2O molecules, and finally forming new, stable hydroxylated active sites for O_3 decomposition on the 2%K-2%Ag/MnO_2 catalyst under humid gas. The O_2^{2-} species on the newly formed active sites (Ag-O(OH)$_x$-K) of 2%K-2%Ag/MnO_2 catalyst are easier to desorb than those on the initial active sites (Ag$_2$O-K) of the 2%K-2%Ag/MnO_2 catalyst and on the active sites (Ag$_2$O) of 2%Ag/MnO_2 catalyst, so the hydroxylated active sites are stable during O_3 decomposition, which means that the 2%K-2%Ag/MnO_2 catalyst can stably decompose O_3 under humid gas.

4. Conclusions

In summary, the stability of 2%Ag/MnO_2 catalysts for O_3 decomposition was significantly improved by simply adding alkali metals. Under relative humidity of 65% and a high weight space velocity of 1680 L·g^{-1}·h^{-1}, the O_3 conversion of 2%K (Rb or Cs)− 2%Ag/MnO_2 catalysts at 30 ℃ was still over 80% after 60 h, which is more than 10 times higher than that of the 2%Ag/MnO_2 catalyst. The addition of alkali metal induces the formation of new hydroxylated active sites on the 2%K-2%Ag/MnO_2 catalyst under humid gas, and O_2^{2-} species on the newly formed active sites (Ag-O(OH)$_x$-K) are easier to desorb than those on the initial active sites (Ag$_2$O-K) of the 2%K-2%Ag/MnO_2 catalyst and on the active sites (Ag$_2$O) of the 2%Ag/MnO_2 catalyst, so the hydroxylated active sites are stable during humid O_3 decomposition. These factors are the key to the stable O_3 decomposition activity of 2%K-2% Ag/MnO_2 catalyst under humid gas. In addition, the effect of alkali metals on Ag nanoparticles was determined. Alkali metals interact with Ag atoms through oxygen bridges, forming the structure Ag-O-K (Rb or Cs), and donate electrons to Ag active sites, forcing Ag active sites on 2% K-2%Ag/MnO_2 catalyst to become hydroxylated by promoting the dissociation of H_2O molecules. The promotion effect of alkali metals on the stability of Ag/MnO_2 catalysts for O_3 decomposition can act as a guidance of the design and synthesis of high-stability catalysts for O_3 decomposition.

CRediT authorship contribution statement

Li Xiaotong: Conceptualization, Data curation, Funding acquisition, Investigation, Writing – original draft. **He Hong:** Conceptualization, Data curation, Funding acquisition, Project administration, Supervision, Writing – review & editing. **Ma Jinzhu:** Conceptualization, Data curation, Funding acquisition, Project administration, Supervision, Writing – review & editing. **Wang Zhisheng:** Investigation, Writing – review & editing. **He Guangzhi:** Formal analysis, Writing – review & editing.

Declaration of Competing Interest

The authors declare that they have no known competing financial interests or personal relationships that could have appeared to influence the work reported in this paper.

Data Availability

Data will be made available on request.

Ackowledgments

Appendix A. Supporting information

Supplementary data associated with this article can be found in the online version at doi:10.1016/j.apcatb.2024.123736.

References

[1] Q. Xiao, G. Geng, T. Xue, S. Liu, C. Cai, K. He, Q. Zhang, Tracking PM$_{2.5}$ and O$_3$ pollution and the related health burden in China 2013-2020, Environ. Sci. Technol. 56 (2022) 6922–6932.

[2] R. Atkinson, Atmospheric chemistry of VOCs and NO$_x$, Atmos. Environ. 34 (2000) 2063–2101.

[3] N.A. Kelly, R.F. Gunst, Response of ozone to changes in hydrocarbon and nitrogen-oxide concentrations in outdoor smog chambers filled with los-angeles air, Atmos. Environ. 24 (1990) 2991–3005.

[4] X.T. Li, J.Z. Ma, H. He, Recent advances in catalytic decomposition of ozone, J. Environ. Sci. 94 (2020) 14–31.

[5] M.O. Fadeyi, Ozone in indoor environments: research progress in the past 15 years, Sustain. Cities Soc. 18 (2015) 78–94.

[6] N. Britigan, A. Alshawa, S.A. Nizkorodov, Quantification of ozone levels in indoor environments generated by ionization and ozonolysis air purifiers, J. Air Waste Manag. Assoc. 56 (2006) 601–610.

[7] S. Bhangar, S.C. Cowlin, B.C. Singer, R.G. Sextro, W.W. Nazaroff, Ozone levels in passenger cabins of commercial aircraft on North American and transoceanic routes, Environ. Sci. Technol. 42 (2008) 3938–3943.

[8] C. Weisel, C.J. Weschler, K. Mohan, J. Vallarino, J.D. Spengler, Ozone and ozone byproducts in the cabins of commercial aircraft, Environ. Sci. Technol. 47 (2013) 4711–4717.

[9] Y. Zou, X. Liu, T. Zhu, M. Tian, M. Cai, Z. Zhao, H. Wu, Simultaneous removal of NO$_x$ and SO$_2$ by MgO combined with O$_3$ oxidation: the influencing factors and O$_3$ consumption distributions, ACS Omega 4 (2019) 21091–21099.

[10] R. Ji, J. Wang, W. Xu, X. Liu, T. Zhu, C. Yan, J. Song, Study on the key factors of NO oxidation using O$_3$: the oxidation product composition and oxidation selectivity, Ind. Eng. Chem. Res. 57 (2018) 14440–14447.

[11] J. Ma, C. Wang, H. He, Transition metal doped cryptomelane-type manganese oxide catalysts for ozone decomposition, Appl. Catal. B: Environ. 201 (2017) 503–510.

[12] X.T. Li, J.Z. Ma, L. Yang, G.Z. He, C.B. Zhang, R.D. Zhang, H. He, Oxygen vacancies induced by transition metal doping in gamma-MnO$_2$ for highly efficient ozone decomposition, Environ. Sci. Technol. 52 (2018) 12685–12696.

[13] J.B. Jia, P.Y. Zhang, L. Chen, Catalytic decomposition of gaseous ozone over manganese dioxides with different crystal structures, Appl. Catal. B: Environ. 189 (2016) 210–218.

[14] G.X. Zhu, J.G. Zhu, W.J. Jiang, Z.J. Zhang, J. Wang, Y. Zhu, Q.F. Zhang, Surface oxygen vacancy induced alpha-MnO$_2$ nanofiber for highly efficient ozone elimination, Appl. Catal. B: Environ. 209 (2017) 729–737.

[15] G. Zhu, W. Zhu, Y. Lou, J. Ma, W. Yao, R. Zong, Y. Zhu, Encapsulate α-MnO$_2$ nanofiber within graphene layer to tune surface electronic structure for efficient ozone decomposition, Nat. Commun. 12 (2021) 4152.

[16] S. Liu, J. Ji, Y. Yu, H. Huang, Facile synthesis of amorphous mesoporous manganese oxides for efficient catalytic decomposition of ozone, Catal. Sci. Technol. 8 (2018) 4264–4273.

[17] Y. Yu, S.L. Liu, J. Ji, H.B. Huang, Amorphous MnO$_2$ surviving calcination: an efficient catalyst for ozone decomposition, Catal. Sci. Technol. 9 (2019) 5090–5099.

[18] W. Hong, J. Ma, T. Zhu, H. He, H. Wang, Y. Sun, F. Shen, X. Li, To enhance water resistance for catalytic ozone decomposition by fabricating H$_2$O adsorption-site in OMS-2 tunnels, Appl. Catal. B: Environ. 297 (2021) 120466.

[19] W. Hong, M. Shao, T. Zhu, H. Wang, Y. Sun, F. Shen, X. Li, To promote ozone catalytic decomposition by fabricating manganese vacancies in ε-MnO$_2$ catalyst via selective dissolution of Mn-Li precursors, Appl. Catal. B: Environ. 274 (2020) 119088.

[20] Y.J. Yang, J.B. Jia, Y. Liu, P.Y. Zhang, The effect of tungsten doping on the catalytic activity of α-MnO$_2$ nanomaterial for ozone decomposition under humid condition, Appl. Catal. A: Gen. 562 (2018) 132–141.

[21] L. Zhang, S. Wang, C. Ni, M. Wang, S. Wang, Ozone elimination over oxygen-deficient MnO$_x$ based catalysts: Effect of different transition metal dopants, Chem. Eng. Sci. 229 (2021) 116011.

[22] G. Zhu, J. Zhu, W. Li, W. Yao, R. Zong, Y. Zhu, Q. Zhang, Tuning the K$^+$ concentration in the tunnels of α-MnO$_2$ to increase the content of oxygen vacancy for ozone elimination, Environ. Sci. Technol. 52 (2018) 8684–8692.

[23] W. Hong, T. Zhu, Y. Sun, H. Wang, X. Li, F. Shen, Enhancing oxygen vacancies by introducing Na$^+$ into OMS-2 tunnels to promote catalytic ozone decomposition, Environ. Sci. Technol. 53 (2019) 13332–13343.

[24] W. Dai, B. Zhang, B. Ji, B. Liu, R. Xie, Y. Gan, X. Xie, J. Zhang, P. Huang, H. Huang, Exceptional ozone decomposition over δ-MnO$_2$/AC under an entire humidity environment, Environ. Sci. Technol. 57 (2023) 17727–17736.

[25] Z. Wu, P. Zhang, S. Rong, J. Jia, Creating water-resistant oxygen vacancies in δ-MnO$_2$ by chlorine introduction for catalytic ozone decomposition at ambient temperature, Appl. Catal. B: Environ. 335 (2023) 122900.

[26] W. Li, G.V. Gibbs, S.T. Oyama, Mechanism of ozone decomposition on a manganese oxide catalyst. I. In situ Raman spectroscopy and ab initio molecular orbital calculations, J. Am. Chem. Soc. 120 (1998) 9041–9046.

[27] W. Qu, M. Luo, Z. Tang, T. Zhong, H. Zhao, L. Hu, D. Xia, S. Tian, D. Shu, C. He, Accelerated catalytic ozonation in a mesoporous carbon-supported atomic Fe-N(4) sites nanoreactor: confinement effect and resistance to poisoning, Environ. Sci. Technol. 57 (2023) 13205–13216.

[28] W. Qu, Z. Tang, S. Tang, H. Wen, J. Fang, Q. Lian, D. Shu, C. He, Cation substitution induced d-band center modulation on cobalt-based spinel oxides for catalytic ozonation, Adv. Funct. Mater. 33 (2023) 2301677.

[29] W. Qu, Z. Tang, H. Wen, M. Luo, T. Zhong, Q. Lian, L. Hu, S. Tian, C. He, D. Shu, Electron transfer trade-offs in MOF-derived cobalt-embedded nitrogen-doped carbon nanotubes boost catalytic ozonation for gaseous sulfur-containing VOC elimination, ACS Catal. 13 (2022) 692–705.

[30] X.T. Li, J.Z. Ma, C.B. Zhang, R.D. Zhang, H. He, Facile synthesis of Ag-modified manganese oxide for effective catalytic ozone decomposition, J. Environ. Sci. 80 (2019) 159–168.

[31] X.T. Li, J.Z. Ma, H. He, Tuning the chemical state of silver on Ag-Mn catalysts to enhance the ozone decomposition performance, Environ. Sci. Technol. 54 (2020) 11566–11575.

[32] X. Li, G. He, J. Ma, X. Shao, Y. Chen, H. He, Boosting the dispersity of metallic Ag nanoparticles and ozone decomposition performance of Ag-Mn catalysts via manganese vacancy-dependent metal-support interactions, Environ. Sci. Technol. 55 (2021) 16143–16152.

[33] H.P. Bonzel, Alkali-promoted gas adsorption and surface reactions on metals, J. Vac. Sci. Technol. A 2 (1984) 866–872.

[34] H. Xin, S. Linic, Analyzing relationships between surface perturbations and local chemical reactivity of metal sites: Alkali promotion of O₂ dissociation on Ag(111), J. Chem. Phys. 144 (2016) 234704.

[35] X.Y. Chen, M. Chen, G.Z. He, F. Wang, G.Y. Xu, Y.B. Li, C.B. Zhang, H. He, Specific role of potassium in promoting Ag/Al₂O₃ for catalytic oxidation of formaldehyde at low temperature, J. Phys. Chem. C 122 (2018) 27331–27339.

[36] Y. Zhai, D. Pierre, R. Si, W. Deng, P. Ferrin, A.U. Nilekar, G. Peng, J.A. Herron, D. C. Bell, H. Saltsburg, M. Mavrikakis, M. Flytzani-Stephanopoulos, Alkali-stabilized Pt-OHₓ species catalyze low-temperature water-gas shift reactions, Science 329 (2010) 1633–1636.

[37] C.F. Huo, B.S. Wu, P. Gao, Y. Yang, Y.W. Li, H. Jiao, The mechanism of potassium promoter: enhancing the stability of active surfaces, Angew. Chem. Int. Ed. 50 (2011) 7403–7406.

[38] C. Zhang, F. Liu, Y. Zhai, H. Ariga, N. Yi, Y. Liu, K. Asakura, M. Flytzani-Stephanopoulos, H. He, Alkali-metal-promoted Pt/TiO₂ opens a more efficient pathway to formaldehyde oxidation at ambient temperatures, Angew. Chem. Int. Ed. 51 (2012) 9628–9632.

[39] M. Yang, S. Li, Y. Wang, J.A. Herron, Y. Xu, L.F. Allard, S. Lee, J. Huang, M. Mavrikakis, M. Flytzani-Stephanopoulos, Catalytically active Au-O(OH)ₓ-species stabilized by alkali ions on zeolites and mesoporous oxides, Science 346 (2014) 1498–1501.

[40] B. Bai, J. Li, Positive effects of K⁺ ions on three-dimensional mesoporous Ag/Co₃O₄ catalyst for HCHO oxidation, ACS Catal. 4 (2014) 2753–2762.

[41] L. Ma, C.Y. Seo, X.Y. Chen, J.H. Li, J.W. Schwank, Sodium-promoted Ag/CeO₂ nanospheres for catalytic oxidation of formaldehyde, Chem. Eng. J. 350 (2018) 419–428.

[42] G. Kresse, J. Furthmuller, Efficient iterative schemes for ab initio total-energy calculations using a plane-wave basis set, Phys. Rev. B 54 (1996) 11169–11186.

[43] G. Kresse, D. Joubert, From ultrasoft pseudopotentials to the projector augmented-wave method, Phys. Rev. B 59 (1999) 1758–1775.

[44] J.P. Perdew, K. Burke, M. Ernzerhof, Generalized gradient approximation made simple, Phys. Rev. Lett. 77 (1997) 3865–3868.

[45] S. Grimme, Semiempirical GGA-type density functional constructed with a long-range dispersion correction, J. Comput. Chem. 27 (2006) 1787–1799.

[46] W.H. Yang, Z.A. Su, Z.H. Xu, W.N. Yang, Y. Peng, J.H. Li, Comparative study of α-, β-, γ- and δ-MnO₂ on toluene oxidation: oxygen vacancies and reaction intermediates, Appl. Catal. B Environ. 260 (2020) 118150.

[47] M. Kitson, R.M. Lambert, Basic studies of the oxygen chemistry of silver: oxygen, dioxygen and superoxide on potassium-dosed Ag(100), Surf. Sci. 109 (1981) 60–74.

[48] Z. Li, J.-Y. Fu, Y. Feng, C.-K. Dong, H. Liu, X.-W. Du, A silver catalyst activated by stacking faults for the hydrogen evolution reaction, Nat. Catal. 2 (2019) 1107–1114.

[49] R.M. Fang, M. He, H.B. Huang, Q.Y. Feng, J. Ji, Y.J. Zhan, D.Y.C. Leung, W. Zhao, Effect of redox state of Ag on indoor formaldehyde degradation over Ag/TiO₂ catalyst at room temperature, Chemosphere 213 (2018) 235–243.

[50] G. Henkelman, A. Arnaldsson, H. Jónsson, A fast and robust algorithm for Bader decomposition of charge density, Comp. Mater. Sci. 36 (2006) 354–360.

[51] S. Imamura, M. Ikebata, T. Ito, T. Ogita, Decomposition of ozone on a silver catalyst, Ind. Eng. Chem. Res. 30 (1991) 217–221.

[52] A. Naydenov, P. Konova, P. Nikolov, F. Klingstedt, N. Kumar, D. Kovacheva, P. Stefanov, R. Stoyanova, D. Mehandjiev, Decomposition of ozone on Ag/SiO₂ catalyst for abatement of waste gases emissions, Catal. Today 137 (2008) 471–474.

[53] P. Nikolov, K. Genov, P. Konova, K. Milenova, T. Batakliev, V. Georgiev, N. Kumar, D.K. Sarker, D. Pishev, S. Rakovsky, Ozone decomposition on Ag/SiO₂ and Ag/clinoptilolite catalysts at ambient temperature, J. Hazard. Mater. 184 (2010) 16–19.

[54] P. Konova, A. Naydenov, P. Nikolov, N. Kumar, Low-temperature ozone decomposition, CO and iso-propanol combustion on silver supported MCM-41 and silica, J. Porous Mat. 25 (2018) 1301–1308.

[55] J. Ma, Y. Chen, G. He, H. He, A robust H-transfer redox mechanism determines the high-efficiency catalytic performance of layered double hydroxides, Appl. Catal. B: Environ. 285 (2021).

[56] Y. Fan, F. Wang, R. Li, C. Liu, Q. Fu, Surface hydroxyl-determined migration and anchoring of silver on alumina in oxidative redispersion, ACS Catal. 13 (2023) 2277–2285.

[57] F. Wang, J. Ma, S. Xin, Q. Wang, J. Xu, C. Zhang, H. He, X. Cheng Zeng, Resolving the puzzle of single-atom silver dispersion on nanosized gamma-Al₂O₃ surface for high catalytic performance, Nat. Commun. 11 (2020) 529.

[58] J.A. Rodriguez, E.R. Remesal, P.J. Ramirez, I. Orozco, Z.Y. Liu, J. Graciani, S. D. Senanayake, J.F. Sanz, Water gas shift reaction on K/Cu(111) and Cu/K/TiO₂(110) surfaces: alkali promotion of water dissociation and production of H₂, ACS Catal. 9 (2019) 10751–10760.

[59] C.H. Liu, R.T. Li, F. Wang, K. Li, Y.M. Fan, R.T. Mu, Q. Fu, Water promoted structural evolution of Ag nanocatalysts supported on alumina, Nano Res. 16 (2023) 9107–9115.